JCTC Journal of Chemical Theory and Computation

pubs.acs.org/JCTC Article

Low-Scaling *GW* Algorithm Applied to Twisted Transition-Metal Dichalcogenide Heterobilayers

Maximilian Graml, Klaus Zollner, Daniel Hernangómez-Pérez, Paulo E. Faria Junior, and Jan Wilhelm*

Cite This: *J. Chem. Theory Comput.* 2024, 20, 2202−2208 Read Online

ABSTRACT: The *GW* method is widely used for calculating the electronic band structure of materials. The high computational cost of *GW* algorithms prohibits their application to many systems of interest. We present a periodic, low-scaling, and highly efficient *GW* algorithm that benefits from the locality of the Gaussian basis and the polarizability. The algorithm enables G_0W_0 calculations on a $MoSe_2/WS_2$ bilayer with 984 atoms per unit cell, in 42 h using 1536 cores. This is 4 orders of magnitude faster than a plane-wave G_0W_0 algorithm, allowing for unprecedented computational studies of electronic excitations at the nanoscale.

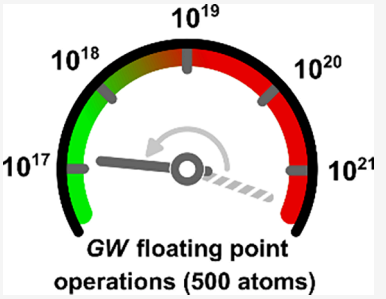

1. INTRODUCTION

Electronic excitations in matter play a pivotal role in various physical phenomena, including light absorption and transport. The characteristics of these excitations are strongly influenced by the host material. Excitons, which are bound electron−hole pairs, exhibit a remarkable and unusually strong electron−hole binding in low-dimensional semiconductors that have emerged in the past decade.[1] When stacking two atomically thin semiconductors on top of each other, the atomic alignment between the layers can exhibit periodic variations, leading to a new type of in-plane superlattice known as the moiré superlattice. Excitons in moiré structures have gained enormous attention recently[2−12] thanks to their highly unusual exciton properties which include spatial confinement due to the moiré potential,[2] interlayer,[5,6] and intralayer charge transfer.[9] Furthermore, electronic properties of moiré lattices can be tuned by the band alignment and the twist angle between the layers such that moiré structures hold great promise as an exciting platform for probing electronic and photonic quantum phenomena over the next decade.[12]

Gaining insight into excitons in moiré structures can be achieved through a combination of experiments, theoretical models, and computations. As an example, low-angle $MoSe_2/WS_2$ moiré structures have shown an interesting interplay of intra- and interlayer exciton hybridization because of the nearly degenerate conduction bands of the $MoSe_2$ and WS_2 layers. The conduction band offset and the wave function hybridization between layers, however, are still under debate.[3,7,13−15] Detailed knowledge about the electronic band structure of the $MoSe_2/WS_2$ moiré bilayer and the implications for exciton formation and binding is thus crucial to resolving this controversy.

In this work, we focus on the *GW* method from many-body perturbation theory,[16−18] which is an approximation for the electronic self-energy that allows for computing the electronic band structure of a given material. Importantly, *GW* accounts for the nonlocal, frequency-dependent screening of the interaction between electrons, which is crucial in moiré bilayers. The *GW* band structure is then the basis for the description of excitons via the Bethe−Salpeter equation.[17,19] Currently available plane-wave-based *GW* algorithms are, however, incapable of treating low-angle moiré cells that contain thousands of atoms,[20] despite their computational scalability to the largest supercomputers.[21−25] Stochastic *GW* methods[26] may enable large-scale *GW* calculations; however, it remains uncertain as to whether applying periodic boundary conditions[27] within the framework of stochastic *GW* can be achieved seamlessly.[28] To compute the *GW* band structure in large moiré cells, the pristine unit-cell matrix projection (PUMP) has been suggested.[9,20] PUMP is based on expanding the moiré cell wave functions in terms of the pristine unit-cell wave functions. By construction, PUMP cannot capture the nanometer-scale atomic reconstruction of moiré structures which can dramatically influence their electronic band structure.[4]

The *GW* space−time method[29] offers a promising route toward large-scale *GW* calculations. This is because the computational scaling is reduced from $O(N_{at}^4 N_k^2)$ for standard *GW* algorithms to $O(N_{at}^3 N_k)$ in the *GW* space−time method, where N_{at} is the number of atoms in the unit cell and N_k is the

Received: November 6, 2023
Revised: December 30, 2023
Accepted: January 8, 2024
Published: February 14, 2024

https://doi.org/10.1021/acs.jctc.3c01230
J. Chem. Theory Comput. 2024, 20, 2202−2208

number of k points used to discretize the Brillouin zone. To achieve the scaling reduction, it is required to use a spatially local basis instead of plane waves. The local basis can be chosen as a real-space grid where studies of unit cells of up to 100 atoms have been reported.[29,30] Another choice of the spatially local basis is an atomic-orbital-like basis.[31] This choice is highly efficient in the GW space−time method, enabling GW calculations on molecules with more than 1000 atoms.[32−36]

Periodic boundary conditions in the GW space−time method with atomic-orbital-like basis functions have not yet been reported. The main inhibiting factor has been the inclusion of k-dependent Coulomb interactions which represent a major challenge regarding computational efficiency and numerical precision.[37−39] In this work, we overcome this challenge by employing real space representations of the polarizability, the screened Coulomb interaction, and the self-energy. The real-space representation allows us to use the minimum image convention (MIC)[40,41] (i.e., each atomic orbital in the simulation interacts only with the closest image of another atomic orbital). We benchmark the algorithm on G_0W_0 band gaps of monolayer MoS_2, $MoSe_2$, WS_2, and WSe_2, finding an average deviation of only 0.06 eV from reference calculations.[42,43] We also apply the GW algorithm to a $MoSe_2$/WS_2 bilayer with an unprecedented cell size of 984 atoms which has an order of magnitude more atoms than previous state-of-the-art large-scale GW calculations.[25]

2. ALGORITHM

The GW algorithm presented in this work starts from a density functional theory (DFT) calculation,

$$\hat{h}_{\mathrm{KS}}(\mathbf{k})\psi_{n\mathbf{k}}(\mathbf{r}) = \varepsilon_{n\mathbf{k}}\psi_{n\mathbf{k}}(\mathbf{r}) \tag{1}$$

where $\varepsilon_{n\mathbf{k}}$ represents the eigenvalues of the Kohn−Sham Hamiltonian $\hat{h}_{\mathrm{KS}}(\mathbf{k})$. Bloch orbitals $\psi_{n\mathbf{k}}$ are expanded in Gaussians,[44]

$$\psi_{n\mathbf{k}}(\mathbf{r}) = \sum_{\mu} C_{n\mu}(\mathbf{k}) \sum_{\mathbf{R}} e^{i\mathbf{k}\cdot\mathbf{R}} \phi_{\mu}^{\mathbf{R}}(\mathbf{r}) \tag{2}$$

where the molecular orbital coefficients $C_{\mu n}(\mathbf{k})$ are optimized in DFT and $\phi_{\mu}^{\mathbf{R}}(\mathbf{r})$ are Gaussian-type basis functions being centered on an atom in cell $\mathbf{R}$.

Following the GW space−time method,[29] we compute the Green's function in imaginary time at the Γ point,[32]

$$\begin{aligned} G_{\mu\nu}(\mathbf{k}=\mathbf{0}, i\tau) = {} & \theta(\tau) \sum_{a}^{\mathrm{virt}} C_{a\mu}(\mathbf{k}=\mathbf{0}) C_{a\nu}(\mathbf{k}=\mathbf{0}) \exp(-(\varepsilon_{a\mathbf{k}=0} - \varepsilon_{\mathrm{F}})\tau) \\ & - \theta(-\tau) \sum_{i}^{\mathrm{occ}} C_{i\mu}(\mathbf{k}=\mathbf{0}) C_{i\nu}(\mathbf{k}=\mathbf{0}) \exp(-(\varepsilon_{i\mathbf{k}=0} - \varepsilon_{\mathrm{F}})\tau) \end{aligned} \tag{3}$$

The irreducible polarizability $\chi_{PQ}(i\tau)$ at $\mathbf{k} = \mathbf{0}$ in the Gaussian auxiliary basis $\{\varphi_P^{\mathbf{R}}(\mathbf{r})\}$ follows,[35]

$$\chi_{PQ}(\mathbf{k}=\mathbf{0}, i\tau) = \sum_{\lambda\nu\mu\sigma} (\mu\nu|P) G_{\mu\lambda}(\mathbf{k}=\mathbf{0}, -i\tau)(\lambda\sigma|Q) G_{\nu\sigma}(\mathbf{k}=\mathbf{0}, i\tau) \tag{4}$$

using three-center matrix elements

$$(\mu\nu|P) = \sum_{\mathbf{R}_1\mathbf{R}_2} \int d\mathbf{r}\, d\mathbf{r}'\, \phi_{\mu}^{\mathbf{R}_1}(\mathbf{r})\, \phi_{\nu}^{\mathbf{R}_2}(\mathbf{r})\, V_{r_c}(\mathbf{r}, \mathbf{r}')\, \varphi_P^{\mathbf{0}}(\mathbf{r}') \tag{5}$$

of the truncated Coulomb operator

$$V_{r_c}(\mathbf{r}, \mathbf{r}') = \begin{cases} 1/|\mathbf{r} - \mathbf{r}'| & \text{if } |\mathbf{r} - \mathbf{r}'| \le r_c, \\ 0 & \text{else} \end{cases} \tag{6}$$

with cutoff radius r_c. The tensor $(\mu\nu|P)$ can be understood as originating from the resolution of the identity with the truncated Coulomb metric (RI-tCm),[35,45,46] where r_c is typically chosen to be 3 Å.[35,46,47] The locality of $V_{r_c}(\mathbf{r}, \mathbf{r}')$ ensures that the tensor $(\mu\nu|P)$ is sparsely occupied, making the GW algorithm computationally efficient. RI-tCm ensures that the resolution of the identity quickly converges with the size of the auxiliary basis $\{\varphi_P^{\mathbf{R}}(\mathbf{r})\}$.[35,45,46] We use Tikhonov regularization[48] for the RI expansion to prevent linear dependencies of fit coefficients, as we discuss in detail in the Supporting Information.

The polarizability $\chi_{PQ}(\mathbf{k}, i\tau)$ is needed on a dense k-point mesh because it is later multiplied with the bare Coulomb interaction $V(\mathbf{k})$ that diverges at the Γ point and thus requires a fine k-point sampling. The atom-centered basis allows us to decompose the Γ-point result (eq 4), $\chi_{PQ}(\mathbf{k} = \mathbf{0}, i\tau)$, using

$$\chi_{PQ}(\mathbf{k}=\mathbf{0}, i\tau) = \sum_{\mathbf{R}} \chi_{PQ}^{\mathbf{R}}(i\tau), \quad \chi_{PQ}^{\mathbf{R}} = \langle \varphi_P^{\mathbf{0}} | \chi | \varphi_Q^{\mathbf{R}} \rangle \tag{7}$$

where $\chi_{PQ}^{\mathbf{R}}$ is the real-space representation of the irreducible polarizability and $\varphi_P^{\mathbf{R}}$ denotes an auxiliary Gaussian orbital which is localized in cell $\mathbf{R}$. For nonmetallic systems, the polarizability $\chi(\mathbf{r}, \mathbf{r}', i\tau)$ is space-local (i.e., $\chi(\mathbf{r}, \mathbf{r}', i\tau)$ exponentially decays with increasing $|\mathbf{r} - \mathbf{r}'|$).[49,50] The matrix element $\chi_{PQ}^{\mathbf{R}}$ thus vanishes in the case of a large distance between the center of $\varphi_P^{\mathbf{0}}$ and the center of $\varphi_Q^{\mathbf{R}}$. We employ MIC (i.e., we assume that $\chi_{PQ}^{\mathbf{R}}(i\tau)$ in eq 7 is nonzero only if the atomic center of $\varphi_P^{\mathbf{0}}$ and the atomic center of $\varphi_Q^{\mathbf{R}}$ are closest together among all cells $\mathbf{R}$). In this way, we extract $\chi_{PQ}^{\mathbf{R}}(i\tau)$ from eq 7,

$$\chi_{PQ}^{\mathbf{R}}(i\tau) = \begin{cases} \chi_{PQ}(\mathbf{k}=\mathbf{0}, i\tau) & \text{if } \varphi_P^{\mathbf{0}},\ \varphi_Q^{\mathbf{R}} \text{ closest among all } \{\mathbf{R}\}, \\ 0 & \text{else} \end{cases} \tag{8}$$

which is exact in the limit of a large, nonmetallic unit cell. Using eq 8, we obtain the polarizability at any k point at negligible computational cost,

$$\chi_{PQ}(\mathbf{k}, i\tau) = \sum_{\mathbf{R}} e^{-i\mathbf{k}\cdot\mathbf{R}} \chi_{PQ}^{\mathbf{R}}(i\tau) \tag{9}$$

We transform the irreducible polarizability to an imaginary frequency,[29,30,51]

$$\chi_{PQ}(\mathbf{k}, i\omega) = \int d\tau \cos(\omega\tau)\, \chi_{PQ}(\mathbf{k}, i\tau) \tag{10}$$

We have observed that $\chi_{PQ}(\mathbf{k}, i\omega)$ computed from eq 10 features spurious negative eigenvalues with small absolute values. The reason is that eq 9 together with eq 8 is exact only in the limit of large unit cells. We remove negative eigenvalues from $\chi_{PQ}(\mathbf{k}, i\omega)$, which requires costly diagonalization for every

https://doi.org/10.1021/acs.jctc.3c01230
J. Chem. Theory Comput. 2024, 20, 2202−2208

k point and every frequency point ω. Once having a positive definite matrix $\chi_{PQ}(\mathbf{k}, i\omega)$, we compute the dielectric function

$$\epsilon(\mathbf{k}, i\omega) = \mathbf{Id} - \mathbf{V}^{0.5}(\mathbf{k})\,\mathbf{M}^{-1}(\mathbf{k})\,\chi(\mathbf{k}, i\omega)\,\mathbf{M}^{-1}(\mathbf{k})\,\mathbf{V}^{0.5}(\mathbf{k}) \tag{11}$$

where $\mathbf{Id}$ is the identity matrix and the truncated Coulomb matrix $\mathbf{M}(\mathbf{k})$ appears due to the RI-tCm,

$$M_{PQ}(\mathbf{k}) = \sum_{\mathbf{R}} e^{-i\mathbf{k}\cdot\mathbf{R}} \int d\mathbf{r}\, d\mathbf{r}'\, \varphi_P^{\mathbf{0}}(\mathbf{r})\, V_{r_c}(\mathbf{r}, \mathbf{r}')\, \varphi_Q^{\mathbf{R}}(\mathbf{r}') \tag{12}$$

We regularize $\mathbf{M}^{-1}(\mathbf{k})$ to prevent linear dependencies in the RI expansion; see details in the Supporting Information.

$\mathbf{V}(\mathbf{k})$ in eq 11 denotes the Coulomb matrix[38,52]

$$V_{PQ}(\mathbf{k}) = \sum_{\mathbf{R}} e^{-i\mathbf{k}\cdot\mathbf{R}} \int d\mathbf{r} d\mathbf{r}'\, \varphi_P^{\mathbf{0}}(\mathbf{r}) \frac{1}{|\mathbf{r} - \mathbf{r}'|} \varphi_Q^{\mathbf{R}}(\mathbf{r}') \tag{13}$$

The sum over $\mathbf{R}$ reaches over the entire crystal. Following the elaborate discussion in the Appendix of ref 52, we evaluate the lattice sum (eq 13) on a finite set of cells $\{\mathbf{R}\}$. The subset fulfills $\sum_{\{\mathbf{R}\}} e^{-i\mathbf{k}\cdot\mathbf{R}} = 0$ for all $\mathbf{k}$ in our k-point mesh to ensure absolute convergence of the lattice sum (eq 13) for 2D periodic systems.[52] Typically, we employ a few thousand neighbor cells to evaluate the lattice sum (eq 13) which is computationally affordable thanks to analytical Coulomb integrals.[53]

We decompose the screened Coulomb interaction $W = V + (\epsilon^{-1} - 1)V$ into the bare Coulomb interaction V and the correction $(\epsilon^{-1} - 1)V$ due to screening. The bare interaction leads to the exchange self-energy Σ^x, and it is well known[54,55] that truncating the bare interaction in Γ-only Hartree−Fock calculations leads to fast convergence in the supercell size. We therefore use the truncated Coulomb operator $V_{r_c^{\mathrm{HF}}}$ from eq 6 for the bare interaction,

$$\mathbf{W}(\mathbf{k}, i\omega) = \mathbf{V}_{r_c^{HF}}(\mathbf{k}) + \mathbf{V}^{0.5}(\mathbf{k})(\epsilon^{-1}(\mathbf{k}, i\omega) - \mathbf{Id})\mathbf{V}^{0.5}(\mathbf{k}) \tag{14}$$

For the cutoff radius r_c^{HF} in eq 14, we set half the minimum of inner box wall distances in periodic directions, which is the common choice in periodic Hartree−Fock calculations.[55]

We transform W to real space,

$$W_{PQ}^{\mathbf{R}}(i\omega) := \langle \varphi_P^{\mathbf{0}} | W(i\omega) | \varphi_Q^{\mathbf{R}} \rangle = \int \frac{d\mathbf{k}}{\Omega_{\mathrm{BZ}}} e^{i\mathbf{k}\cdot\mathbf{R}} W_{PQ}(\mathbf{k}, i\omega) \tag{15}$$

where Ω_{BZ} is the Brillouin zone (BZ) volume. Special care is required for the BZ integral as $W_{PQ}(\mathbf{k}, i\omega)$ diverges at the Γ point with $1/k$ for two-dimensional materials if φ_P and φ_Q are s-type basis functions.[37,38,56] We evaluate $W_{PQ}(\mathbf{k}, i\omega)$ using a 4×4 Monkhorst−Pack k-point mesh[57] $\{\mathbf{k}_j\}_{j=1}^{N_k}$, $N_k = 8$,[58] and a 6×6 Monkhorst−Pack k-point mesh $\{\mathbf{q}_j\}_{j=1}^{N_q}$, $N_q = 18$. We extrapolate the BZ integration (eq 15) with the inverse square root of the number of k points.[38,59] In practice, we extrapolate with respect to k points by discretizing eq 15 to

$$W_{PQ}^{\mathbf{R}}(i\omega) = \sum_{j=1}^{N_q} v_j e^{i\mathbf{q}_j\cdot\mathbf{R}} W_{PQ}(\mathbf{q}_j, i\omega) - \sum_{j=1}^{N_k} w_j e^{i\mathbf{k}_j\cdot\mathbf{R}} W_{PQ}(\mathbf{k}_j, i\omega) \tag{16}$$

where k-point extrapolation is absorbed in integration weights

$$v_j = \frac{1}{(1 - \sqrt{N_k/N_q})N_q}, \quad w_j = \frac{1}{(\sqrt{N_q/N_k} - 1)N_k} \tag{17}$$

Following the GW space−time method,[29,30] we compute the self-energy $\Sigma(\mathbf{r}, \mathbf{r}', i\tau) = iG(\mathbf{r}, \mathbf{r}', i\tau)\, W(\mathbf{r}, \mathbf{r}', i\tau)$.[29] $\Sigma(\mathbf{r}, \mathbf{r}', i\tau)$ is space-local as $G(\mathbf{r}, \mathbf{r}', i\tau)$ is space-local,[49] and only elements of $W(\mathbf{r}, \mathbf{r}', i\tau)$ with small $|\mathbf{r} - \mathbf{r}'|$ contribute to Σ. We thus continue with the minimum image of eq 15

$$W_{PQ}^{\mathrm{MIC}}(i\tau) := W_{PQ}^{\mathbf{R}_{PQ}^{\min}}(i\tau) \tag{18}$$

where the cell vector

$$\mathbf{R}_{PQ}^{\min} = \underset{\mathbf{R}}{\operatorname{argmin}} |\mathbf{R}_P - (\mathbf{R}_Q + \mathbf{R})| \tag{19}$$

gives the smallest distance between the atomic centers $\mathbf{R}_P$ of $\varphi_P^{\mathbf{0}}$ and the atomic center $\mathbf{R}_Q + \mathbf{R}$ of $\varphi_Q^{\mathbf{R}}$. We include the Γ-point RI metric matrix $\mathbf{M}$ from eq 12,

$$\tilde{\mathbf{W}}(i\omega) = \mathbf{M}^{-1}(\mathbf{k} = \mathbf{0})\,\mathbf{W}^{\mathrm{MIC}}(i\omega)\,\mathbf{M}^{-1}(\mathbf{k} = \mathbf{0}) \tag{20}$$

which leads to the self-energy at the Γ point,

$$\Sigma_{\lambda\sigma}(\mathbf{k}=\mathbf{0}, i\tau) = i \sum_{\nu\mu PQ} (\lambda\mu|Q) G_{\mu\nu}(\mathbf{k}=\mathbf{0}, i\tau)(\nu\sigma|P)\tilde{W}_{PQ}(i\tau) \tag{21}$$

k points in Σ follow from MIC at negligible computational cost (cf. eqs 8 and 9),

$$\Sigma_{\mu\nu}(\mathbf{k}, i\tau) = \sum_{\mathbf{R}} e^{i\mathbf{k}\cdot\mathbf{R}} \cdot \begin{cases} \Sigma_{\mu\nu}(\mathbf{k} = \mathbf{0}, i\tau) & \text{if } \phi_\mu^{\mathbf{0}},\ \phi_\nu^{\mathbf{R}} \text{ closest,} \\ 0 & \text{else} \end{cases} \tag{22}$$

We transform the self-energy to real energy[18,29,30,32,35] and to the Bloch basis to compute quasiparticle energies $\varepsilon_{n\mathbf{k}}^{G_0W_0}$,

$$\varepsilon_{n\mathbf{k}}^{G_0W_0} = \varepsilon_{n\mathbf{k}} + \mathrm{Re}\Sigma_{n\mathbf{k}}(\varepsilon_{n\mathbf{k}}^{G_0W_0}) - v_{n\mathbf{k}}^{\mathrm{xc}} \tag{23}$$

where $v_{n\mathbf{k}}^{\mathrm{xc}}$ is the diagonal of the exchange-correlation matrix.

3. NUMERICAL PRECISION

The numerical trick in the presented GW algorithm is the MIC used in eqs 8, 18, and 22. MIC is exact in the limit of a large unit cell. We determine the critical cell size for the validity of MIC by computing the G_0W_0 band gap of monolayers MoS_2, $MoSe_2$, WS_2, and WSe_2, presented in Figure 1. For the four materials, the band gap changes on average by only 11 meV between the 10×10 supercell (300 atoms in the unit cell) and the 14×14 supercell (588 atoms in the unit cell). We conclude that the GW algorithm from this work can be used to study unit cells that are as large as a 10×10 supercell or larger. In the Supporting Information, we show additional convergence tests on the basis set size, the number of time and frequency points, the k-point mesh size, the filter threshold for sparse operations, and the vertical box height.

We compare the G_0W_0 band gap of monolayers MoS_2, $MoSe_2$, WS_2, and WSe_2 to the G_0W_0 band gap computed from three different plane-wave codes;[39,42,43] see Table 1. We find that our G_0W_0 band gaps deviate on average by only 0.06 eV to the band gaps from plane-wave-based codes. This small discrepancy might be due to the use of different pseudopotentials and the difficulty in reaching the complete basis set limit.

https://doi.org/10.1021/acs.jctc.3c01230
J. Chem. Theory Comput. 2024, 20, 2202−2208

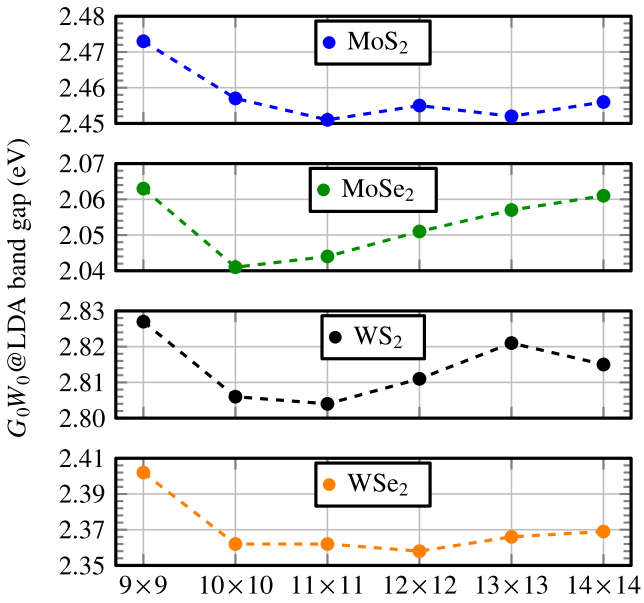

Figure 1. G_0W_0 band gap of monolayer WS_2, MoS_2, WSe_2, and $MoSe_2$ calculated from eq 23 as a function of the supercell size (TZVP-MOLOPT basis set,[60] without spin−orbit coupling (SOC)).

Table 1. G_0W_0@PBE Band Gap (in eV, without SOC) of Monolayers MoS_2, $MoSe_2$, WS_2, and WSe_2 Computed from Equation 23 (TZV2P-MOLOPT Basis,[60] 10 × 10 Supercell, Detailed Convergence Test in the SI) and Computed from Plane-Wave Codes[39,42,43a]

Software package	MoS_2	$MoSe_2$	WS_2	WSe_2
This work (CP2K[61])	2.47	2.07	2.81	2.37
GPAW[42]	2.53	2.12	2.75	2.30
BerkeleyGW[39]	2.45	2.09	2.61	2.34
VASP[43]	2.50	2.06	2.70	2.34

[a]Details of BerkeleyGW calculations are given in the SI. We have removed SOC from the GPAW band gaps.[42].

4. COMPUTATIONAL EFFORT

The presented G_0W_0 algorithm has a significantly reduced computational cost compared to plane-wave-based G_0W_0 algorithms. We show the number of floating point operations to compute the irreducible polarizability χ in a plane-wave G_0W_0 algorithm in Figure 2 in black. As a comparison, we show the execution of our low-scaling G_0W_0 algorithm via green traces. Our G_0W_0 algorithm requires 40,000 times fewer floating point operations for a 14 × 14 supercell as computing χ in plane waves for a 14 × 14 supercell. One might reduce the computational cost for computing χ in plane waves by a stochastic evaluation of the unoccupied band summation.[23] For such an algorithm, the inversion of the dielectric matrix ϵ remains a computationally costly step. As we show in Figure 2, inverting ϵ in a plane-wave basis requires an order of magnitude more floating point operations compared to executing our whole G_0W_0 algorithm.

Further advantages compared to plane-wave-based algorithms include the cheap diagonalization of the Kohn−Sham matrix to obtain Bloch states thanks to the compact Gaussian basis. Also, nonperiodic directions are easily dealt with in our *GW* algorithm by restricting the sum over cells **R** to periodic directions. It is not necessary to truncate the Coulomb operator in nonperiodic directions as in plane-wave algorithms.[39,62] Moreover, the self-energy (eq 22) is available in the full Gaussian basis set, which allows us to compute the G_0W_0 correction for all Bloch states at negligible computational cost.

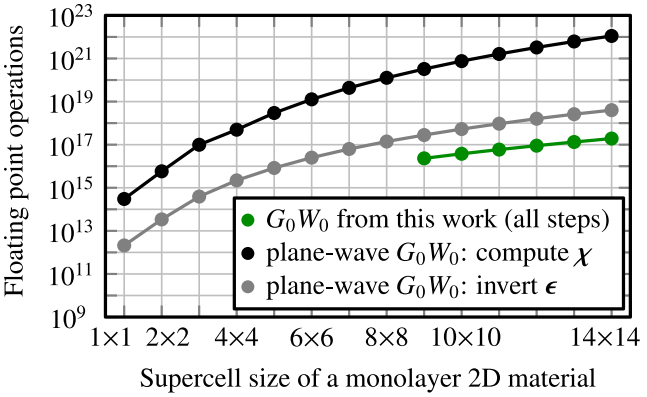

Figure 2. Number of floating point operations (real double precision) needed for executing G_0W_0 algorithms. Green: low-scaling G_0W_0 algorithm from this work using a TZVP-MOLOPT basis set.[60] Black: computing the irreducible polarizability χ in a plane-wave basis. Gray: inverting the dielectric matrix ϵ in a plane-wave basis. Underlying computational parameters are typical for monolayers MoS_2, $MoSe_2$, WS_2, and WSe_2; see the detailed raw data and discussion available in the SI.

We measured the computation time of the algorithm, shown in Figure 3. The computation time is moderate; as an example,

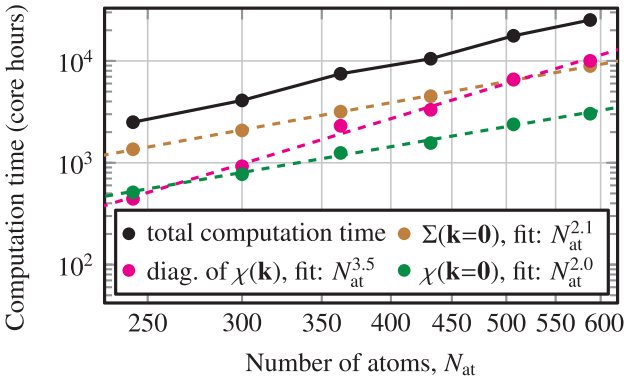

Figure 3. Execution time of a G_0W_0 calculation for $MoSe_2$ 9 × 9−14 × 14 supercells (TZVP-MOLOPT basis set) on Supermuc-NG (Intel Skylake Xeon Platinum 8174). Magenta points show the computational cost to diagonalize the polarizability $\chi(\mathbf{k})$, which allows us to remove all spurious negative eigenvalues of $\chi(\mathbf{k})$ to ensure numerical stability. Dashed lines show a fit of αN_{at}^{β} to the execution time, where α and β are fit parameters. Raw data are available in the SI.

a G_0W_0 calculation on the 10 × 10 $MoSe_2$ supercell (300 atoms) takes only 7 h on 576 cores. Assuming ideal scalability starting from the 9 × 9 cell, we estimate that a G_0W_0 calculation on 4500 atoms is in reach.[63] Scalability improvements are the subject of ongoing work to achieve this system size in practice.

5. APPLICATION: 2D HETEROBILAYER

We now focus on an application of the G_0W_0 algorithm to transition-metal dichalcogenide heterobilayers which recently gained increased attention due to twist-angle-dependent moiré potentials and interlayer excitons.[3,4,7−9,12−15] Recent large-

https://doi.org/10.1021/acs.jctc.3c01230
J. Chem. Theory Comput. 2024, 20, 2202−2208

scale plane-wave-based *GW* calculations on twisted heterostructures were limited to 75 atoms in the unit cell.[25] This *GW* computation[25] has been described to be highly cumbersome, and it was achieved only by using an advanced accelerated large-scale version of the BerkeleyGW code which scales to entire leadership high-performance computers with more than half a million cores.[22,23] Small unit cells with 75 atoms allow for only the study of heterobilayers with selected, large twist angles and absent atomic reconstruction.

In order to illustrate the large-scale capabilities of our G_0W_0 algorithm beyond monolayers, we focus on prototypical $MoSe_2/WS_2$ twisted heterostructures. On one hand, the different lattice parameters of $MoSe_2$ and WS_2 give rise to a considerably large moiré periodicity at zero twist angle (∼8 nm), thus requiring a large number of atoms in the structure. On the other hand, low-angle $MoSe_2/WS_2$ has shown an interesting interplay of intra- and interlayer exciton hybridization because of the nearly degenerate conduction bands. This feature, however, is still under debate in the literature.[3,7,13−15] The underlying electronic structure is thus crucial to resolve this controversy and is exactly the kind of problem that requires large-scale *GW* calculations. Here we considered $MoSe_2/WS_2$ moiré superstructures with twist angles of between 9.3 and 26.6° (Figure 4) that have

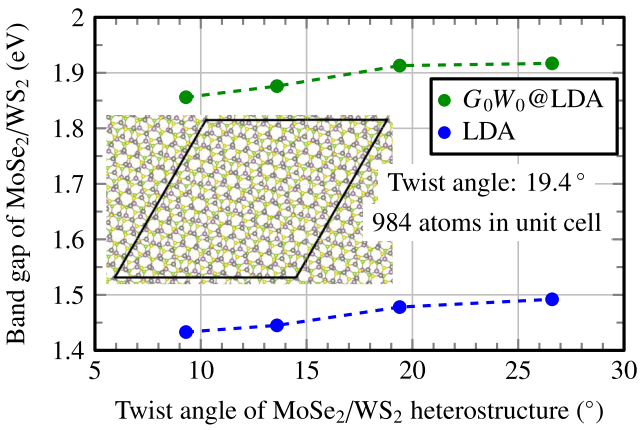

Figure 4. Band gap of a $MoSe_2/WS_2$ heterostructure as a function of the twist angle. Inset: The unit cell (black rhomboid) for a 19.4° twist angle contains 984 atoms.

corresponding unit cells of up to 984 atoms. We emphasize that in all cases the strain of the individual monolayers is <0.01% compared to the experimentally determined lattice constants,[64,65] which is important because the band gap is very sensitive to strain.[66,67] The G_0W_0 band gap of the $MoSe_2/WS_2$ bilayer depends on the twist angle changing from 1.86 eV (9.3°) to 1.92 eV (26.8°), in line with experimental observations of the exciton emission energy.[13] Our *GW* calculation on the 984-atom heterostructure takes 42 h on only 1536 cores, which is a factor of 30,000 faster than with a plane-wave algorithm; see the estimate in the SI. Such large-scale *GW* calculations are an ideal starting point for further analysis of the electronic structure of these materials. For example, with our *GW* algorithm, the calculation of deep moiré potentials[4] is within reach because of atomic reconstruction and height variations. Both crucially influence the interlayer screening that is captured by the *GW* method. On top of a *GW* calculation, the Bethe-Salpeter equation[17,19] will enable the study of excitons in large-scale moiré structures. Our computationally efficient scheme also holds great promise for nanoscale excited-state dynamics in low-dimensional materials with Green's function methods.

6. CONCLUSIONS

We have presented a low-scaling *GW* algorithm with periodic boundary conditions employing localized basis functions and the minimum image convention. The *GW* algorithm is numerically precise and requires up to 5 orders of magnitude fewer floating point operations compared to plane-wave codes. We carried out a G_0W_0 calculation on a $MoSe_2/WS_2$ heterostructure with 984 atoms in the unit cell which is an order of magnitude more than the state of the art.[25] Our *GW* algorithm will enable routine applications of *GW* and its time-dependent variants to low-dimensional, nanostructured materials that were previously computationally highly challenging.

■ ASSOCIATED CONTENT

Data Availability Statement

The low-scaling *GW* algorithm is implemented in the open-source CP2K package,[61] which is freely available from GitHub.[68] Inputs and outputs of the calculations are also available on GitHub.[69]

Supporting Information

The Supporting Information is available free of charge at https://pubs.acs.org/doi/10.1021/acs.jctc.3c01230.

Further computational parameters underlying our calculations (Sec. S1); regularized resolution of the identity used in the *GW* algorithm (Sec. S2); numerical convergence of our benchmark monolayer band gaps (Sec. S3, S4); resolution of the identity with the truncated Coulomb metric in Sec. S5; periodic, low-scaling *GW* algorithm from the manuscript to a *GW* algorithm with standard scaling (Sec. S6); the number of required floating point operations in our low-scaling Gaussian algorithm, a standard-scaling Gaussian algorithm and in planewave algorithms (Sec. S7 − S11); timings of our algorithm (Sec. S12); comparison of the supercell convergence of our algorithm to the supercell convergence of stochastic *GW* (Sec. S13) (PDF)

■ AUTHOR INFORMATION

Corresponding Author

Jan Wilhelm − *Institute of Theoretical Physics and Regensburg Center for Ultrafast Nanoscopy (RUN), University of Regensburg, 93053 Regensburg, Germany;* orcid.org/0000-0001-8678-8246; Email: jan.wilhelm@physik.uni-regensburg.de

Authors

Maximilian Graml − *Institute of Theoretical Physics and Regensburg Center for Ultrafast Nanoscopy (RUN), University of Regensburg, 93053 Regensburg, Germany;* orcid.org/0000-0002-4279-8511

Klaus Zollner − *Institute of Theoretical Physics, University of Regensburg, 93053 Regensburg, Germany*

Daniel Hernangómez-Pérez − *Department of Molecular Chemistry and Materials Science, Weizmann Institute of Science, Rehovot 7610001, Israel;* orcid.org/0000-0002-4277-0236

https://doi.org/10.1021/acs.jctc.3c01230
J. Chem. Theory Comput. 2024, 20, 2202−2208

Paulo E. Faria Junior − *Institute of Theoretical Physics, University of Regensburg, 93053 Regensburg, Germany*

Complete contact information is available at: https://pubs.acs.org/10.1021/acs.jctc.3c01230

Notes

The authors declare no competing financial interest.

■ ACKNOWLEDGMENTS

We thank Mauro Del Ben, Maria Camarasa-Gomez, Ferdinand Evers, Dorothea Golze, Jürg Hutter, Ole Schütt, and Shridhar Shanbhag for helpful discussions. K.Z. and P.E.F.J. acknowledge funding by the Deutsche Forschungsgemeinschaft (DFG, German Research Foundation), SFB 1277 (project no. 314695032, projects B07 and B11), SPP 2244 (project no. 443416183), and the European Union Horizon 2020 Research and Innovation Program under contract number 881603 (Graphene Flagship). D.H.-P. acknowledges support from a Minerva Foundation Grant (7135421), an ERC Starting Grant (101041159), and the DFG through SFB 1277 (no. 314695032, project B10). J.W. acknowledges funding by the DFG via the Emmy Noether Programme (project no. 503985532). The Gauss Centre for Supercomputing is acknowledged for providing computational resources on SuperMUC-NG at the Leibniz Supercomputing Centre under the project ID pn72pa. The Quantum Espresso and BerkeleyGW computations were carried out at the Max Planck Computing and Data Facility Cluster.

■ REFERENCES

(1) Mak, K. F.; Lee, C.; Hone, J.; Shan, J.; Heinz, T. F. Atomically Thin MoS_2: A New Direct-Gap Semiconductor. *Phys. Rev. Lett.* **2010**, *105*, No. 136805.

(2) Seyler, K. L.; Rivera, P.; Yu, H.; Wilson, N. P.; Ray, E. L.; Mandrus, D. G.; Yan, J.; Yao, W.; Xu, X. Signatures of moiré-trapped valley excitons in $MoSe_2/WSe_2$ heterobilayers. *Nature* **2019**, *567*, 66−70.

(3) Zhang, L.; Zhang, Z.; Wu, F.; Wang, D.; Gogna, R.; Hou, S.; Watanabe, K.; Taniguchi, T.; Kulkarni, K.; Kuo, T.; Forrest, S. R.; Deng, H. Twist-angle dependence of moiré excitons in $WS_2/MoSe_2$ heterobilayers. *Nat. Commun.* **2020**, *11*, 5888.

(4) Shabani, S.; Halbertal, D.; Wu, W.; Chen, M.; Liu, S.; Hone, J.; Yao, W.; Basov, D. N.; Zhu, X.; Pasupathy, A. N. Deep moiré potentials in twisted transition metal dichalcogenide bilayers. *Nat. Phys.* **2021**, *17*, 720−725.

(5) Karni, O.; et al. Structure of the moiré exciton captured by imaging its electron and hole. *Nature* **2022**, *603*, 247−252.

(6) Schmitt, D.; et al. Formation of moiré interlayer excitons in space and time. *Nature* **2022**, *608*, 499−503.

(7) Gobato, Y. G.; de Brito, C. S.; Chaves, A.; Prosnikov, M. A.; Woźniak, T.; Guo, S.; Barcelos, I. D.; Milošević, M. V.; Withers, F.; Christianen, P. C. M. Distinctive g-Factor of Moiré-Confined Excitons in van der Waals Heterostructures. *Nano Lett.* **2022**, *22*, 8641−8646.

(8) Barré, E.; Karni, O.; Liu, E.; O'Beirne, A. L.; Chen, X.; Ribeiro, H. B.; Yu, L.; Kim, B.; Watanabe, K.; Taniguchi, T.; Barmak, K.; Lui, C. H.; Refaely-Abramson, S.; da Jornada, F. H.; Heinz, T. F. Optical absorption of interlayer excitons in transition-metal dichalcogenide heterostructures. *Science* **2022**, *376*, 406−410.

(9) Naik, M. H.; et al. Intralayer charge-transfer moiré excitons in van der Waals superlattices. *Nature* **2022**, *609*, 52−57.

(10) Rivera, P.; Yu, H.; Seyler, K. L.; Wilson, N. P.; Yao, W.; Xu, X. Interlayer valley excitons in heterobilayers of transition metal dichalcogenides. *Nat. Nanotechnol.* **2018**, *13*, 1004−1015.

(11) Jin, C.; Ma, E. Y.; Karni, O.; Regan, E. C.; Wang, F.; Heinz, T. F. Ultrafast dynamics in van der Waals heterostructures. *Nat. Nanotechnol.* **2018**, *13*, 994−1003.

(12) Huang, D.; Choi, J.; Shih, C.-K.; Li, X. Excitons in semiconductor moiré superlattices. *Nat. Nanotechnol.* **2022**, *17*, 227−238.

(13) Alexeev, E. M.; et al. Resonantly hybridized excitons in moiré superlattices in van der Waals heterostructures. *Nature* **2019**, *567*, 81−86.

(14) Tang, Y.; Gu, J.; Liu, S.; Watanabe, K.; Taniguchi, T.; Hone, J.; Mak, K. F.; Shan, J. Tuning layer-hybridized moiré excitons by the quantum-confined Stark effect. *Nat. Nanotechnol.* **2021**, *16*, 52−57.

(15) Ma, X.; Fu, S.; Ding, J.; Liu, M.; Bian, A.; Hong, F.; Sun, J.; Zhang, X.; Yu, X.; He, D. Robust Interlayer Exciton in $WS_2/MoSe_2$ van der Waals Heterostructure under High Pressure. *Nano Lett.* **2021**, *21*, 8035−8042.

(16) Hedin, L. New Method for Calculating the One-Particle Green's Function with Application to the Electron-Gas Problem. *Phys. Rev.* **1965**, *139*, A796−A823.

(17) Onida, G.; Reining, L.; Rubio, A. Electronic excitations: density-functional versus many-body Green's-function approaches. *Rev. Mod. Phys.* **2002**, *74*, 601−659.

(18) Golze, D.; Dvorak, M.; Rinke, P. The *GW* Compendium: A Practical Guide to Theoretical Photoemission Spectroscopy. *Front. Chem.* **2019**, *7*, 377.

(19) Blase, X.; Duchemin, I.; Jacquemin, D.; Loos, P.-F. The Bethe−Salpeter Equation Formalism: From Physics to Chemistry. *J. Phys. Chem. Lett.* **2020**, *11*, 7371−7382.

(20) Li, H.; Xiang, Z.; Naik, M. H.; Kim, W.; Li, Z.; Sailus, R.; Banerjee, R.; Taniguchi, T.; Watanabe, K.; Tongay, S.; Zettl, A.; da Jornada, F. H.; Louie, S. G.; Crommie, M. F.; Wang, F. Imaging Moiré Excited States with Photocurrent Tunneling Microscopy. *arXiv 2306.00859*, 2023.

(21) Sangalli, D.; et al. Many-body perturbation theory calculations using the yambo code. *J. Phys.: Condens. Matter* **2019**, *31*, No. 325902.

(22) Del Ben, M.; da Jornada, F. H.; Canning, A.; Wichmann, N.; Raman, K.; Sasanka, R.; Yang, C.; Louie, S. G.; Deslippe, J. Large-scale GW calculations on pre-exascale HPC systems. *Comput. Phys. Commun.* **2019**, *235*, 187−195.

(23) Del Ben, M.; Yang, C.; Li, Z.; Jornada, F. H. d.; Louie, S. G.; Deslippe, J. Accelerating Large-Scale Excited-State GW Calculations on Leadership HPC Systems. *SC20: International Conference for High Performance Computing, Networking, Storage and Analysis* **2020**, 1−11.

(24) Yu, V. W.-Z.; Govoni, M. GPU Acceleration of Large-Scale Full-Frequency GW Calculations. *J. Chem. Theory Comput.* **2022**, *18*, 4690−4707.

(25) Kundu, S.; Amit, T.; Krishnamurthy, H. R.; Jain, M.; Refaely-Abramson, S. Exciton fine structure in twisted transition metal dichalcogenide heterostructures. *Npj Comput. Mater.* **2023**, *9*, 186.

(26) Neuhauser, D.; Gao, Y.; Arntsen, C.; Karshenas, C.; Rabani, E.; Baer, R. Breaking the Theoretical Scaling Limit for Predicting Quasiparticle Energies: The Stochastic *GW* Approach. *Phys. Rev. Lett.* **2014**, *113*, No. 076402.

(27) Brooks, J.; Weng, G.; Taylor, S.; Vlček, V. Stochastic many-body perturbation theory for Moiré states in twisted bilayer phosphorene. *J. Phys.: Condens. Matter* **2020**, *32*, No. 234001.

(28) We discuss challenges in stochastic *GW* calculations on two-dimensional materials in detail in the Supporting Information.

(29) Rojas, H. N.; Godby, R. W.; Needs, R. J. Space-Time Method for Ab Initio Calculations of Self-Energies and Dielectric Response Functions of Solids. *Phys. Rev. Lett.* **1995**, *74*, 1827−1830.

(30) Liu, P.; Kaltak, M.; Klimeš, J.; Kresse, G. Cubic scaling *GW*: Towards fast quasiparticle calculations. *Phys. Rev. B* **2016**, *94*, No. 165109.

(31) Rohlfing, M.; Krüger, P.; Pollmann, J. Efficient scheme for GW quasiparticle band-structure calculations with applications to bulk Si and to the Si(001)-(2 × 1) surface. *Phys. Rev. B* **1995**, *52*, 1905−1917.

(32) Wilhelm, J.; Golze, D.; Talirz, L.; Hutter, J.; Pignedoli, C. A. Toward *GW* Calculations on Thousands of Atoms. *J. Phys. Chem. Lett.* **2018**, *9*, 306−312.
(33) Förster, A.; Visscher, L. Low-Order Scaling G_0W_0 by Pair Atomic Density Fitting. *J. Chem. Theory Comput.* **2020**, *16*, 7381−7399.
(34) Duchemin, I.; Blase, X. Cubic-Scaling All-Electron GW Calculations with a Separable Density-Fitting Space−Time Approach. *J. Chem. Theory Comput.* **2021**, *17*, 2383−2393.
(35) Wilhelm, J.; Seewald, P.; Golze, D. Low-Scaling GW with Benchmark Accuracy and Application to Phosphorene Nanosheets. *J. Chem. Theory Comput.* **2021**, *17*, 1662−1677.
(36) Förster, A.; Visscher, L. Quasiparticle Self-Consistent GW-Bethe−Salpeter Equation Calculations for Large Chromophoric Systems. *J. Chem. Theory Comput.* **2022**, *18*, 6779−6793.
(37) Ren, X.; Merz, F.; Jiang, H.; Yao, Y.; Rampp, M.; Lederer, H.; Blum, V.; Scheffler, M. All-electron periodic G_0W_0 implementation with numerical atomic orbital basis functions: Algorithm and benchmarks. *Phys. Rev. Materials* **2021**, *5*, No. 013807.
(38) Zhu, T.; Chan, G. K.-L. All-Electron Gaussian-Based G_0W_0 for Valence and Core Excitation Energies of Periodic Systems. *J. Chem. Theory Comput.* **2021**, *17*, 727−741.
(39) Qiu, D. Y.; da Jornada, F. H.; Louie, S. G. Screening and many-body effects in two-dimensional crystals: Monolayer MoS_2. *Phys. Rev. B* **2016**, *93*, No. 235435.
(40) Paier, J.; Diaconu, C. V.; Scuseria, G. E.; Guidon, M.; VandeVondele, J.; Hutter, J. Accurate Hartree-Fock energy of extended systems using large Gaussian basis sets. *Phys. Rev. B* **2009**, *80*, 174114.
(41) Irmler, A.; Burow, A. M.; Pauly, F. Robust Periodic Fock Exchange with Atom-Centered Gaussian Basis Sets. *J. Chem. Theory Comput.* **2018**, *14*, 4567−4580.
(42) Gjerding, M. N.; et al. Recent progress of the Computational 2D Materials Database (C2DB). *2D Mater.* **2021**, *8*, No. 044002.
(43) Camarasa-Gómez, M.; Ramasubramaniam, A.; Neaton, J. B.; Kronik, L. Transferable screened range-separated hybrid functionals for electronic and optical properties of van der Waals materials. *Phys. Rev. Mater.* **2023**, *7*, No. 104001.
(44) Blum, V.; Gehrke, R.; Hanke, F.; Havu, P.; Havu, V.; Ren, X.; Reuter, K.; Scheffler, M. Ab initio molecular simulations with numeric atom-centered orbitals. *Comput. Phys. Commun.* **2009**, *180*, 2175−2196.
(45) Jung, Y.; Sodt, A.; Gill, P. M. W.; Head-Gordon, M. Auxiliary basis expansions for large-scale electronic structure calculations. *Proc. Natl. Acad. Sci. U.S.A.* **2005**, *102*, 6692−6697.
(46) Luenser, A.; Schurkus, H. F.; Ochsenfeld, C. Vanishing-Overhead Linear-Scaling Random Phase Approximation by Cholesky Decomposition and an Attenuated Coulomb-Metric. *J. Chem. Theory Comput.* **2017**, *13*, 1647−1655.
(47) We discuss the choice r_c = 3 Å in the Supporting Information.
(48) Goncharsky, A.; Stepanov, V.; Tikhonov, A.; Yagola, A. *Numerical Methods for the Solution of Ill-Posed Problems*; Kluwer Academic Publishers: Dordrecht, 1995.
(49) Kohn, W. Density Functional and Density Matrix Method Scaling Linearly with the Number of Atoms. *Phys. Rev. Lett.* **1996**, *76*, 3168−3171.
(50) Martin, R. M.; Reining, L.; Ceperley, D. M. *Interacting Electrons*; Cambridge University Press, 2016.
(51) Azizi, M.; Wilhelm, J.; Golze, D.; Giantomassi, M.; Panadés-Barrueta, R. L.; Delesma, F. A.; Buccheri, A.; Gulans, A.; Rinke, P.; Draxl, C.; Gonze, X. *J. Open Source Softw.* **2023**, *8*, 5570.
(52) Grundei, M. M. J.; Burow, A. M. Random Phase Approximation for Periodic Systems Employing Direct Coulomb Lattice Summation. *J. Chem. Theory Comput.* **2017**, *13*, 1159−1175.
(53) Golze, D.; Benedikter, N.; Iannuzzi, M.; Wilhelm, J.; Hutter, J. Fast evaluation of solid harmonic Gaussian integrals for local resolution-of-the-identity methods and range-separated hybrid functionals. *J. Chem. Phys.* **2017**, *146*, 034105.
(54) Spencer, J.; Alavi, A. Efficient calculation of the exact exchange energy in periodic systems using a truncated Coulomb potential. *Phys. Rev. B* **2008**, *77*, 193110.
(55) Guidon, M.; Hutter, J.; VandeVondele, J. Robust Periodic Hartree-Fock Exchange for Large-Scale Simulations Using Gaussian Basis Sets. *J. Chem. Theory Comput.* **2009**, *5*, 3010−3021.
(56) Wilhelm, J.; Hutter, J. Periodic *GW* calculations in the Gaussian and plane-waves scheme. *Phys. Rev. B* **2017**, *95*, 235123.
(57) Monkhorst, H. J.; Pack, J. D. Special points for Brillouin-zone integrations. *Phys. Rev. B* **1976**, *13*, 5188−5192.
(58) We employ the k symmetry $\mathbf{k} \leftrightarrow -\mathbf{k}$.
(59) Laughon, K.; Yu, J. M.; Zhu, T. Periodic Coupled-Cluster Green's Function for Photoemission Spectra of Realistic Solids. *J. Phys. Chem. Lett.* **2022**, *13*, 9122−9128.
(60) VandeVondele, J.; Hutter, J. Gaussian basis sets for accurate calculations on molecular systems in gas and condensed phases. *J. Chem. Phys.* **2007**, *127*, 114105.
(61) Kühne, T. D.; et al. CP2K: An electronic structure and molecular dynamics software package - Quickstep: Efficient and accurate electronic structure calculations. *J. Chem. Phys.* **2020**, *152*, 194103.
(62) Hüser, F.; Olsen, T.; Thygesen, K. S. Quasiparticle GW calculations for solids, molecules, and two-dimensional materials. *Phys. Rev. B* **2013**, *87*, 235132.
(63) The computation time is $T = (N_{at}/243)^2 1870$ core hours + $(N_{at}/243)^3 443$ core hours, where we took the execution time of quadratic and cubic steps as shown in Figure 3. The maximum job size on Supermuc-NG is 150 000 cores for 24 h, making 3.6 Mio. core hours, allowing for a G_0W_0 calculation on 4500 atoms.
(64) Schutte, W. J.; De Boer, J. L.; Jellinek, F. Crystal structures of tungsten disulfide and diselenide. *J. Solid State Chem.* **1987**, *70*, 207−209.
(65) James, P. B.; Lavik, M. T. The crystal structure of $MoSe_2$. *Acta Crystallogr.* **1963**, *16*, 1183−1183.
(66) Zollner, K.; Junior, P. E. F.; Fabian, J. Strain-tunable orbital, spin-orbit, and optical properties of monolayer transition-metal dichalcogenides. *Phys. Rev. B* **2019**, *100*, 195126.
(67) Chaves, A.; et al. Bandgap engineering of two-dimensional semiconductor materials. *npj 2D Mater. Appl.* **2020**, *4*, 29.
(68) https://github.com/cp2k/cp2k, accessed December 20, 2023.
(69) https://github.com/JWilhelm/Inputs_outputs_low_scaling_GW_TMDC, accessed December 20, 2023.

https://doi.org/10.1021/acs.jctc.3c01230
J. Chem. Theory Comput. 2024, 20, 2202−2208